Nano Energy 78 (2020) 105337

Contents lists available at ScienceDirect

Nano Energy

journal homepage: http://www.elsevier.com/locate/nanoen

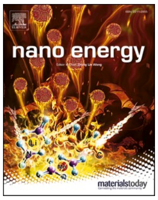

Bioinspired, multifunctional dual-mode pressure sensors as electronic skin for decoding complex loading processes and human motions

Ye Qiu [a,b,1], Ye Tian [a,b,1], Shenshen Sun [a,b], Jiahui Hu [a,b], Youyan Wang [a,b], Zheng Zhang [a,b], Aiping Liu [c,**], Huanyu Cheng [d,***], Weizhan Gao [e], Wenan Zhang [e], Hao Chai [f], Huaping Wu [a,b,*]

[a] *College of Mechanical Engineering, Zhejiang University of Technology, Hangzhou, 310023, China*
[b] *Key Laboratory of Special Purpose Equipment and Advanced Processing Technology, Ministry of Education and Zhejiang Province, Zhejiang University of Technology, Hangzhou, 310023, China*
[c] *Center for Optoelectronics Materials and Devices, Zhejiang Sci-Tech University, Hangzhou, 310018, China*
[d] *Department of Engineering Science and Mechanics, The Pennsylvania State University, University Park, PA, 16802, USA*
[e] *College of Information Engineering, Zhejiang University of Technology, Hangzhou, 310023, China*
[f] *Zhijiang College of Zhejiang University of Technology, Shaoxing 312030, China*

ARTICLE INFO

Keywords:
Dual-mode pressure sensor
Pyramid microstructures
Deconvolution of complex loading processes and motions
Human-machine interfaces

ABSTRACT

Mimicry of the somatosensory system in the human skin via electronic devices exhibits broad applications in intelligent robotics and wearable electronics. Here, we report a novel biomimetic flexible dual-mode pressure sensor that is based on the interlocked piezoelectric and piezoresistive films with pyramid microstructures. The sensitivity of the sensor is significantly enhanced because of the induced larger stain variation along the thickness direction of the former piezoelectric film and increased contact area in the latter piezoresistive film. The synergistic effect of the piezoelectric and piezoresistive responses to stimuli also allows the dual-mode sensor to detect over broad pressure and frequency ranges. The analysis of these signals can deconvolute multiple aspects of the complex stimuli loading processes, including their loading direction, rate, magnitude, and duration. As a proof-of-concept demonstration, the dual-mode pressure sensor is successfully integrated with manipulators and human bodies to decode the complex and delicate picking processes and human motions, respectively. When combined with the other sensing modalities, the multifunctional dual-mode pressure sensor delivers new application opportunities in intelligent soft robotics and human-machine interfaces.

1. Introduction

As a delicate sensory organ of the human body, the skin could sense multiple spatiotemporal tactile stimuli of various frequencies and intensities through different types of tactile receptors. In particular, the slowly adapting receptors (i.e., Merkel and Ruffini corpuscles) respond to static stimuli on the skin, which helps sense the pressure during grasping processes. Meanwhile, the fast-adapting receptors (i.e., Meissner and Pacinian corpuscles) can detect dynamic stimuli, ranging from texture discrimination in low-frequency (5–50 Hz) to vibration in high-frequency (up to 400 Hz) [1–4]. Broad pressure range includes subtle pressure (e.g., a light brush of <100 Pa) and large pressure (e.g., pulse pressure and gentle touch of 1–10 kPa) can also be perceived by hair follicles (HF) and C-fibre low-threshold mechanoreceptors (LTMs).

Simultaneous detection of static and dynamic mechanical stimuli over a large pressure range in a relatively linear manner is of critical significance for flexible electronic skins in interactive human-machine interfaces, including smart prosthesis, medical rehabilitation, and humanoid robotics [5–14]. Early efforts exploit piezoresistive or capacitive sensors for the static and low-frequency mechanical stimuli and piezoelectric or triboelectric sensors for the dynamic and high-frequency stimuli [15–22]. The former relies on a continuous electrical response of active sensing elements, whereas the latter merely responds to high-frequency stimuli via instantaneous charge generation [2,23–29].

---

* Corresponding author.College of Mechanical Engineering, Zhejiang University of Technology, Hangzhou, 310023, China.
** Corresponding author.
*** Corresponding author.
E-mail addresses: liuaiping1979@gmail.com (A. Liu), Huanyu.Cheng@psu.edu (H. Cheng), wuhuaping@gmail.com (H. Wu).
[1] Y. Qiu and Y. Tian contributed equally to this work.

https://doi.org/10.1016/j.nanoen.2020.105337
Received 12 June 2020; Received in revised form 11 August 2020; Accepted 28 August 2020

Additional efforts on novel materials and designs of micro/-nanostructures have demonstrated improvement in limit/range of detection and sensitivity due to the easy deformation of high surface area structure [30,31]. For instance, interlocked micropillars [31], graded intrafillable microstructures [32], and multilayer interlocked geometry [33] can significantly increase the maximum sensing pressure range with boosted sensitivity. However, it is still challenging to simultaneously detect the pressure over a wide magnitude and frequency range in high sensitivity with a single-mode sensor.

Various methods have been investigated to extend the sensing capability, and one representative effort is to explore dual-mode sensors for simultaneous monitoring of various stimuli [34–37]. Among them, exploiting the integration of two transduction modes (e.g., nanowires/graphene heterostructures, hierarchical micro-/nano-structured ZnO nanowire arrays, and piezoelectric PVDF/graphene sandwiches) [38–45] can simultaneously detect the magnitudes of static and dynamic stimuli by combining the piezoelectric with piezoresistive modes. However, these studies only focus on the simple combination of the magnitudes of measured stimuli, without further exploration of the sensing capability. For instance, the direction and rate of change in the stimuli are not readily available from the piezoresistive mode, whereas the piezoelectric mode cannot distinguish the reverse loading from the unloading process. Realizing the full potential of the dual-mode sensors hinges on the comprehensive analysis of the measured signals. The motion direction, operating rate, and real-time attitude are required for up-to-date intelligent robots to adapt and work in the complex, dynamics, and sometimes extreme environments [46]. However, the existing dual-mode sensing modules are not sufficient, and they lack the aforementioned information to do so, thereby limiting their applications in laboratory settings. Thus, it is highly desirable to develop and demonstrate a dual-mode pressure sensor with extended capabilities to capture the missing information (e.g., the direction, rate, and magnitude of dynamic and static stimuli) for future robots and human-machine interfaces.

Here, we report a comprehensive set of theoretical/numerical design tools and fabrication schemes to quantitatively elucidate the sensing

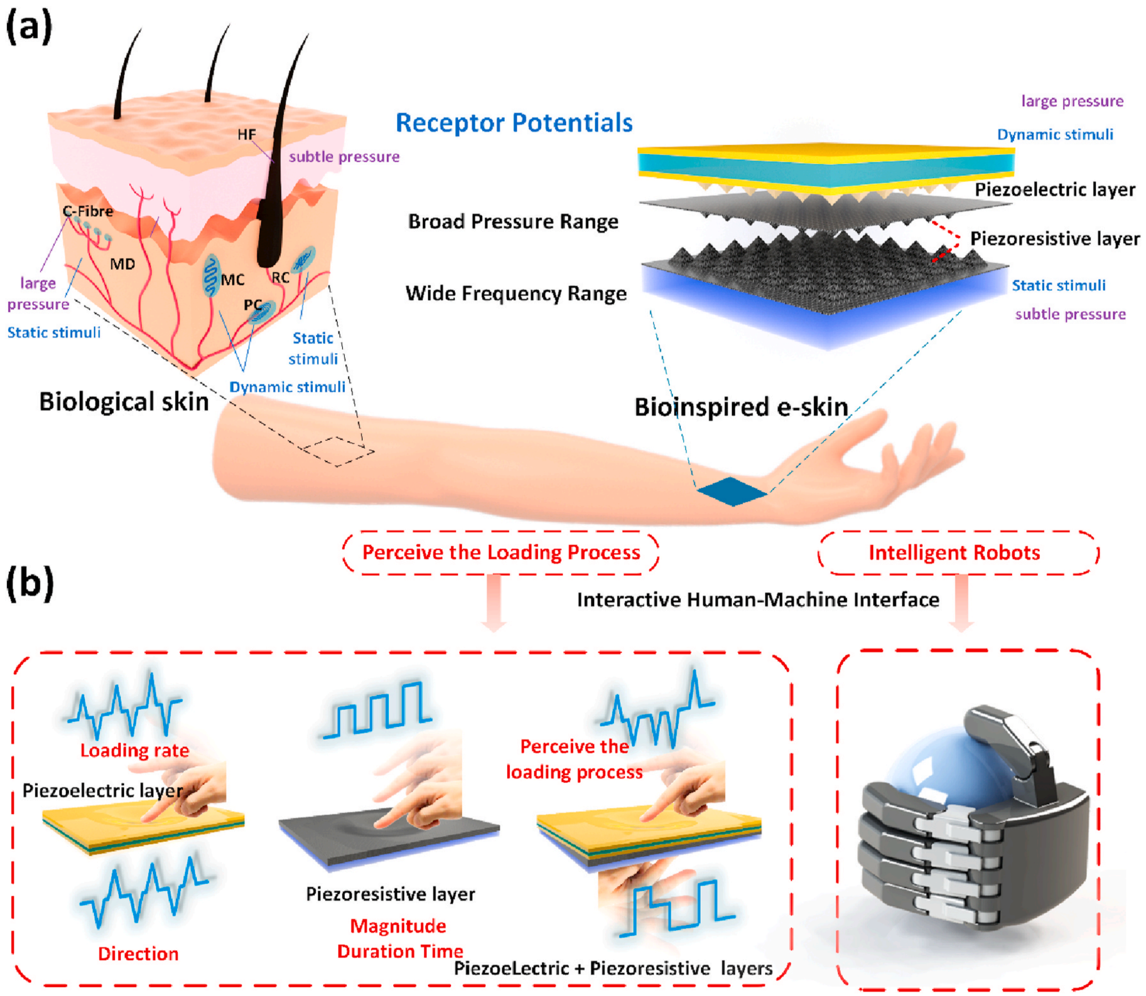

Fig. 1. Human skin-inspired multifunctional dual-mode pressure sensor. a) Schematic illustrations of the structure of human skin and the multifunctional dual-mode pressure sensor in exploded view. Human skin consists of slow-adapting mechanoreceptors [Merkel (MD) and Ruffini corpuscles (RE)] for static stimuli, fast-adapting mechanoreceptors [Meissner (MC) and Pacinian corpuscles (PC)] for dynamic stimuli, hair follicles (HF) for subtle pressure, C-fibre low-threshold mechanoreceptors (LTMs) for large pressure, respectively. The multifunctional dual-mode pressure sensor is composed of two flexible sensing layers for piezoelectric and piezoresistive modes: the piezoelectric layer mimics the fast-adapting mechanoreceptors (i.e., MC and PC) to sense the high-frequency dynamic stimuli. The interlocked piezoresistive layers capture the static stimuli to emulate the slow-adapting mechanoreceptors (i.e., MD and RE). The interlocked pyramid microstructures mimic those on the human skin to help increase the sensitivity due to their modulation in the stress distribution and contact area. The synergistic effect of the piezoelectric and piezoresistive films allows the dual-mode sensor to work over a broad pressure magnitude range to emulate the function of HF and C-fibre LTMs in the human skin. b) The complex loading process can be accurately captured by combining the dynamic loading rate and direction detected by the piezoelectric layer with the magnitude and duration measured by the piezoresistive layer. This capability opens up new application opportunities for the dual-mode pressure sensors in interactive human-machine interfaces and intelligent robots.

mechanism and demonstrate the unique application opportunities of dual-mode pressure sensors with piezoelectric and piezoresistive layers. The surface relief pyramid microstructures are designed for both the piezoelectric P(VDF-TrFE) film and piezoresistive rGO arrays in the dual-mode pressure sensors, in which the unique architecture contributes to a large stain variation along the thickness of the former piezoelectric film and increased contact area to the latter piezoresistive array for enhanced sensitivity. The synergistic effect of piezoelectric and piezoresistive materials yields a flexible dual-mode pressure sensor with high sensitivity over an exceptionally broad pressure range (0.015–9 kPa) and linear response in a wide frequency range (0–700 Hz). Most importantly, combining the dynamic loading rate and direction measured by the piezoelectric layer with the magnitude and duration measured by the piezoresistive layer results in the unique capability to capture the complex loading process. The real-time measurement of the dynamically changing stimuli with the dual-mode pressure sensors is further demonstrated as sensitive manipulators and precise motion decoders for future human-machine interfaces.

2. Results and discussion

Inspired by the structures and physiological functions of the human skin, a dual-mode electronic-skin (e-skin) is demonstrated with flexible and microstructured piezoelectric and piezoresistive layers (Fig. 1). The top piezoelectric film in the e-skin mimics the perceptive function of the fast-adapting receptors in the human skin to detect high-frequency dynamic stimuli, whereas the bottom piezoresistive module captures static pressures similar to the slow-adapting mechanoreceptors. The piezoresistive module relies on the change in contact resistance between two rGO arrays with interlocked micro-pyramids. The interlocked pyramid microstructures mimic those on the human skin to help increase the sensitivity due to their modulation in the stress distribution and contact area. Meanwhile, the synergistic effect of the piezoelectric and piezoresistive films allows the dual-mode e-skin to work over a broad pressure magnitude range to emulate the function of HF and C-fibre LTMs in the human skin. Most importantly, the complex loading process can be accurately captured by combining the dynamic loading rate and direction detected by the piezoelectric layer with the magnitude and duration measured by the piezoresistive layer. This capability opens up new application opportunities for the dual-mode pressure sensors in interactive human-machine interfaces.

The pressure loaded on the piezoelectric film generates the piezoelectric voltage, according to the piezoelectric theory. Constitutive models have been proposed to establish relations among the stress σ_{ij}, strain ε_{ij}, electrical field E_i, and electrical displacement D_{ij}, where c_{ij}, e_{ij}, and k_{ij} are the elastic, piezoelectric, and dielectric constants, respectively. The coordinate x_1 is defined along the longitudinal direction, x_2 is along the width direction, and x_3 is along the thickness direction (also the piezoelectric polarization direction). Considering that a uniaxial compressive force F applied along the x_3 direction on a flat piezoelectric film with an area of A, the voltage V across its thickness l measured by a voltmeter with an inner resistance of R is obtained as [47].

$$V=\frac{(-\bar{e})l}{\bar{k}}\frac{\sigma_{33}}{\bar{E}}-\frac{(-\bar{e})l^2}{AR\left(\bar{k}\right)^2}e^{\frac{lt}{AR\bar{k}}}\int_0^t\frac{\sigma_{33}}{\bar{E}}e^{\frac{lt}{AR\bar{k}}}dt, \tag{1}$$

where $F = F_{\max}[1 - cos(2\pi ft)]/2$ is a periodic function of time t, $\bar{e} = e_{33} - [2c_{13}/(c_{11} + c_{12})]e_{31}$ and $\bar{k} = k_{33} + [2c_{33}e_{31}^2 - 4c_{13}e_{31}e_{33} + (c_{11} + c_{12})e_{33}^2]/(c_{11}c_{33} + c_{12}c_{33} - 2c_{13}^2)$ are the effective piezoelectric constants, $\bar{E} = c_{33} - 2c_{13}^2/(c_{11} + c_{12})$. The material parameters of P(VDF-TrFE) are as follows: $c_{11} = 1.6 \times 10^9$ N/m^2; $c_{12} = 0.8 \times 10^9$ N/m^2; $c_{13} = 1.42 \times 10^9$ N/m^2; $c_{33} = 1.63 \times 10^9$ N/m^2; $e_{31} = 0.032$ C/m^2; $e_{33} = -0.02$ C/m^2; $k_{33} = 1.6 \times 10^{-10}$ F/m [48]. While the tailoring of microstructures have been demonstrated as an effective means to increase the voltage output and piezoelectric sensor response [49], their precise effect remains elusive. The systematic study involves the role of piezoelectric films with a surface relief of periodic cylindrical, truncated hemispherical, and truncated pyramidal microstructures, all with the same base area of A_0 (Fig. S1, Supporting Information). Quantitative analysis of piezoelectric output under pressure is carried out by changing the side length ratio of the bottom to top. The average stress in all three microstructural unit along the thickness (i.e., x_3) can be expressed as

$$\sigma_{33}=\frac{mF}{A_0}, \tag{2}$$

where $m = a_2/a_1$, a_1 and a_2 are the side lengths at the top and base of the microstructures ($m = 1$ for cylindrical microstructures). Since the calculated voltage is across the thickness direction, the voltage is mainly related to the film thickness, base area, and top area. Because the voltage output from the piezoelectric films is dominated by the microstructures, it can then be expressed as

$$V=\frac{(-\bar{e})l}{\bar{k}}\frac{\sigma_{33}}{\bar{E}}-\frac{(-\bar{e})l^2}{A_0R\left(\bar{k}\right)^2}e^{\frac{lt}{AR\bar{k}}}\int_0^t\frac{\sigma_{33}}{\bar{E}}e^{\frac{lt}{AR\bar{k}}}dt. \tag{3}$$

According to the SEM image of the surface morphology of the prepared pyramidal microstructures (inset of Fig. S1c, Supporting Information), the m value in the pyramidal microstructures is 10. The hemispherical microstructures prepared by following the method in the previous literature report [50] leads to a choice of 5 for the m value. The theoretical calculation results show that the thin film with a pyramid-shaped structure has a large voltage output compared to the cylinder- and hemisphere-shaped micropatterned thin films under the same pressure, which is further confirmed by the ABAQUS simulation (Fig. 2a). Compared to the cylinder- and hemisphere-shaped microstructures, the film with a pyramid-shaped structure has a larger stress/strain variation along the thickness direction and therefore gives higher piezoelectric output, which is consistent with the previously reported results on pressure sensors with different microstructures (e.g., cylindrical, hemispherical, pyramidal microstructures) [51].

The piezoresistive sensor relies on the pressure-induced resistance change. The total resistance R of each sensing unit is composed of three parts [50,52]: the resistances of the top electrode (R_{CE}), contact interface (R_{CI}), and bottom electrode (R_{BE}), i.e.,

$$R=R_{TE}+R_{CI}+R_{BE}=\rho_{\mathrm{G}}\left(\frac{L_{\mathrm{TE}}}{A_{\mathrm{G}}}+\frac{d_{\mathrm{G}}}{A_{\mathrm{CI}}}+\frac{L_{\mathrm{BE}}}{A_{\mathrm{G}}}\right) \tag{4}$$

where the ρ_{G} is resistivity, L_{TE} and L_{BE} are the length of graphene in the top and bottom layer of each sensing unit, d_{G} is the thickness, A_{CI} is contact area, A_{G} is the cross-sectional area of graphene film. As the piezoresistive layers act as electrodes with sufficiently small resistance, the total resistive change is dominated by the contact interface resistance between the top and bottom graphene layers. The contact interface resistance is mainly contributed by the change of the contact area A_{CI} in response to pressure, which is simulated in the piezoresistive films with three microstructures (Fig. 2b). Compared to the cylinder- and hemisphere-shaped microstructures, the pyramidal microstructures induce a larger local stress concentration at the contact, and the stress intensity increases as the normal pressure increases. The deformation of the pyramidal microstructures induced by the local stress further causes a larger increase in the contact area, contributing to the enhanced sensitivity. Therefore, the results indicate that films with pyramid microstructures can help improve the sensing performance of both the piezoelectric and piezoresistive sensors.

Based on these results, thin films with pyramid-shaped microstructures and the optimal designs obtained by the theoretical and numerical studies have been explored in the following experimental investigations. Because the larger pyramid microstructures arranged in a higher density array are found to increase the measurement range and output voltage of the sensor [53], the micro-pyramid array with a hemline length of 60 μm

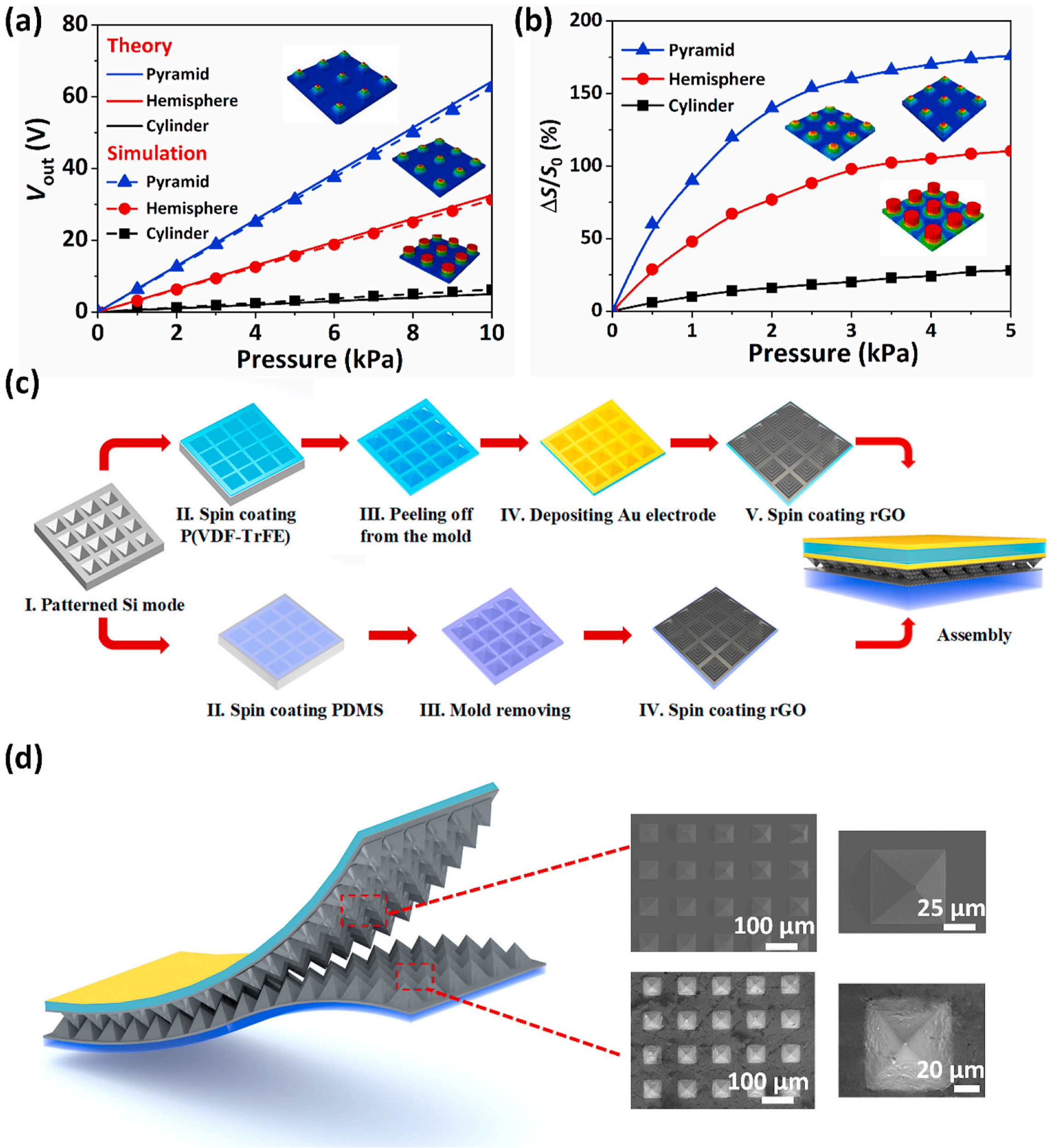

Fig. 2. Theoretical and numerical analyses of the influence of microstructures on the piezoelectric and piezoresistive sensing performance. a) A comparison of the voltage output between the theoretical predictions and simulation results as a function of the applied pressure for the piezoelectric film with different microstructures (the voltage drop across the piezoelectric film with cylindrical, hemispherical, pyramidal microstructures shown in the insets). b) Simulation results of the change in contact area as a function of the applied pressure between the piezoresistive films with different microstructures (the stress distributions of the piezoresistive film with cylindrical, hemispherical, pyramidal microstructures shown in the insets). c) Schematic illustration of the fabrication process for the dual-mode sensor. d) Top view of the scanning electron microscopy (SEM) images of the pyramidal microstructure on the piezoelectric and piezoresistive layers.

and pitch size of 60 μm is selected without increasing fabrication complexity. The height of 42 μm is then determined since an angle of 54.7° forms between the slanted plane and square from the wet etching process of the Si mold. The same Si mold is used to prepare both the piezoelectric and piezoresistive components in the dual-mode sensor (Fig. 2c). In brief, peeling off the cured piezoelectric P(VDF-TrFE) and PDMS films from the Si mold provides the film with the identical microstructures. The formation of polar phases in P(VDF-TrFE) films was confirmed by X-ray diffraction (XRD) and Fourier transform infrared spectroscopy (FTIR) analyses (Figs. S2a and b, Supporting Information). The deposition of Au electrodes on both sides of the piezoelectric P(VDF-TrFE) film with the pyramidal microstructures leads to the piezoelectric module. The rGO solution was fabricated using a two-step freeze-drying and thermal annealing method. Raman spectra of GO and rGO revealed two peaks at 1340 cm^{-1} and 1590 cm^{-1}, corresponding to the D band and G band, respectively (Fig. S2c, Supporting Information). The normalized relative current change ($\Delta I/I_0$) of the piezoresistive sensor without microstructure (i.e., planar piezoresistive layers) was demonstrated to depend on the rGO loading concentration (Fig. S3a, Supporting Information). The rGO loading concentration of 0.75 mg/mL was selected due to the highest sensitivity for sensing the pressure and bending (Fig. S3, Supporting Information). The resistance change from the piezoresistive sensor can be associated with either the applied pressure or the bending stress, thus, decoupling the current changes from the bending stress and the applied pressure has remained a daunting challenge. Representative strategies to address this challenge include 1) minimizing the effect from one (e.g., strain [54] or pressure [55]), 2) allow the sensor to exhibit different structural changes upon pressure and strain [56], 3) exploiting multiple sensors in the array [57]. We further show the measured $\Delta I/I_0$ characteristics according to the applied pressure while the bending stress is applied, the sensor with an applied bending strain of 1 % can still clearly distinguish the applied pressure of 1, 2, and 3 kPa in the measured $\Delta I/I_0$ characteristics (Fig. S4, Supporting Information). In the next step, the spin coating of the rGO on its side with the microstructure prepares the top piezoresistive electrode. After the spin coating of the rGO on the side of the PDMS with the microstructure, assembling it with the above piezoelectric P(VDF-TrFE) layer forms an interlocking structure. The pyramid microstructuresare uniformly distributed with high precision, as indicated in the scanning electron microscopy (SEM) images (Fig. 2d).

Evaluation of the fabricated dual-mode sensor (Fig. 3) indicates the minimum detectable pressure from the piezoelectric mode is 100 Pa, whereas the one from the piezoresistive mode is 15 Pa (Fig.3a and Figs. S5a and b, Supporting Information). Although the piezoresistive mode can detect the pressure up to 4 kPa with a high sensitivity of 14.5 kPa^{-1} (Fig. 3b), the response saturates for the higher applied pressure (i.e., above 4 kPa) (Fig. S5c, Supporting Information). The sensitivity is also observed to be higher than those from their interlocked counterparts with either cylinder-shaped (6.8 kPa^{-1}) or hemisphere-shaped microstructures (10.1 kPa^{-1}) [44]. In contrast, the piezoelectric voltage continues to increase rapidly as the pressure increases from 4 kPa to 9 kPa (Fig. S5d, Supporting Information). In fact, the piezoelectric mode maintains a high sensitivity of 1.62 V/kPa^{-1}in the broad pressure range from 100 Pa to 9 kPa (Fig. 3b), which agrees reasonably well with Eq. (3) for the applied pressure up to 10 kPa (Fig. S6, Supporting Information). The deviation for the applied pressure above 10 kPa comes from the fact that the theory does not account for the maximum number of dipoles that could orient in the piezoelectric material. The difference in the range of detection between two modes comes from the respective sensing mechanisms of piezoresistive and piezoelectric sensors. A small pressure at the interface of contacting graphene pyramids would generate a friction force that results in a controlled yet rapid increase in the contact area and measured current, leading to the sensitive piezoresistive sensors for detecting pressures at the lower range [58,59]. As the pressure gradually increases, the increase in the contact area slows down and eventually saturates so that the piezoresistive sensors reach their detection limit. In contrast, the centers of both positive and negative charge carriers are not fully separated for a smaller applied pressure,

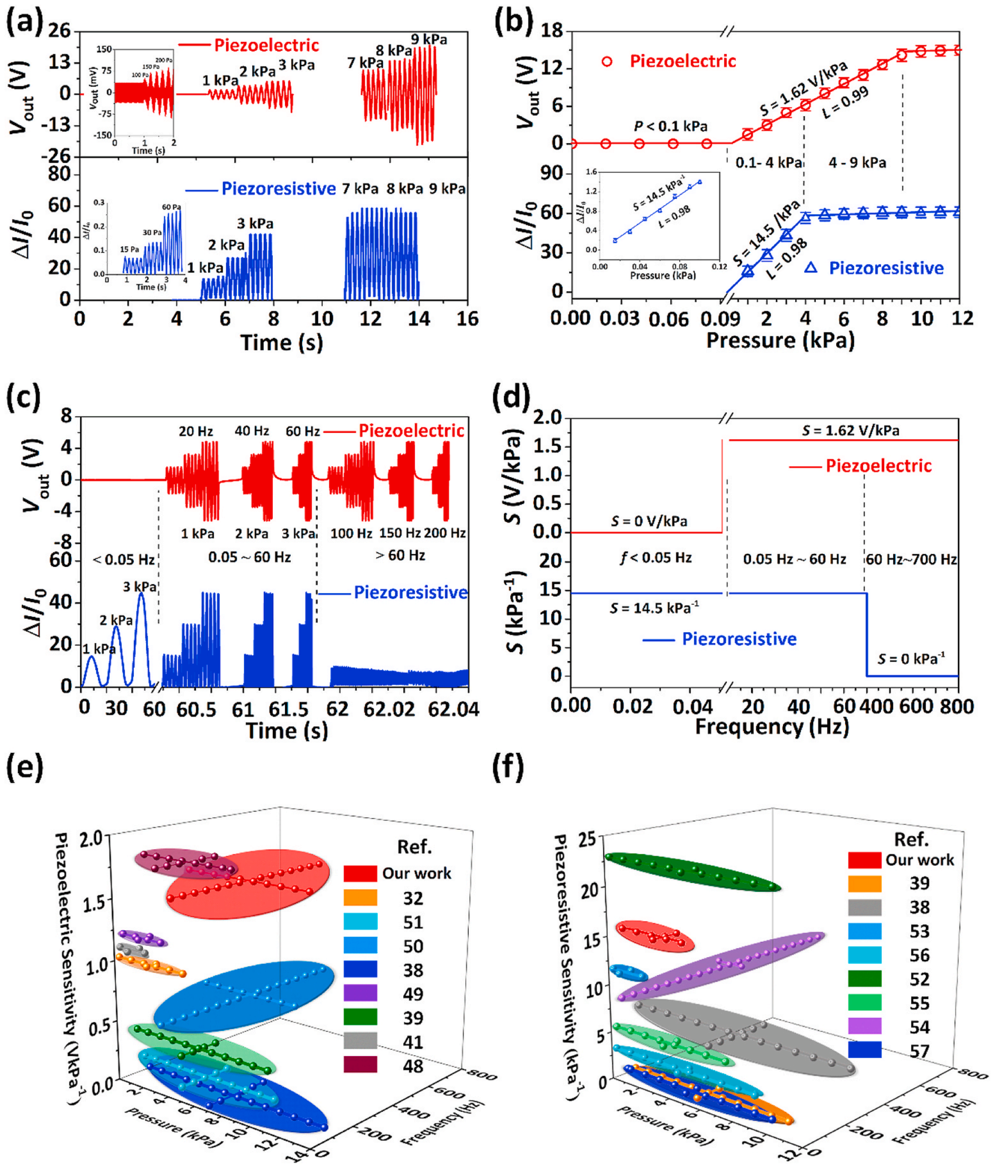

Fig. 3. Pressure and frequency sensing demonstrations of the dual-mode sensors. a) Pressure sensing range of dual-mode sensors. b) The sensitivity of dual-mode sensors for the applied pressure from 0 to 12 kPa. c) Frequency sensing range of dual-mode sensors. d) The sensitivity of dual-mode sensors as the frequency of the applied pressure increases from 0 to 800 Hz. Comparison in the sensitivity and linear sensing ranges between this work and previous literature reports for the e) piezoelectric and f) piezoresistive modes.

resulting in a small piezoelectric potential. The increase in the applied pressure results in a further separation between the centers of positive and negative charge carriers before reaching a maximum value (i.e., the maximum number of dipoles that could orient in one direction), corresponding to the upper limit in the pressure range [60]. The observed difference in the range of detection between two modes from this study is also consistent with the recently reported results (e.g., 6.8 kPa^{-1} in [0.6, 13] kPa for the piezoresistive mode and 0.006 V/kPa in [40, 17.4] kPa for the piezoelectric mode [44]. In addition to high sensitivity, both sensing modes exhibit excellent linearity, i.e., 0.98 over the entire pressure range from 15 Pa to 4 kPa for the piezoresistive mode and 0.99 over the range from 100 Pa to 9 kPa for the piezoelectric mode (Fig. 3b), likely attributed to the interlocked pyramid microstructures. The role of the interlocked pyramid microstructure on the enhanced sensitivity and linearity has been further confirmed by a direct comparison between three piezoresistive sensors: 1) with the interlocked pyramid-shaped microstructure array, 2) with single-sided pyramid-shaped microstructure array, and 3) without microstructures. The sensor with the interlocked pyramid-shaped microstructure array indeed shows much higher sensitivity and linearity than the other two (Fig. S7, Supporting Information). Together, the dual-mode sensor demonstrates a highly linear sensing performance over a broad pressure range (15 Pa-9 kPa) for monitoring diverse stimuli in from a low to high pressure, which can cover most of the range for the medium pulse pressure and gentle touch (1–10 kPa), as indicated in the previous literature reports [33].

Detecting various vibration and sound waves over a wide frequency range is also crucial for the electronic sensor to mimic the equ capability of the human skin. The piezoresistive mode can readily detect the static or low-frequency (e.g., below 0.05 Hz) pressure (Fig.3c and Fig. S8a, Supporting Information), but it becomes challenging as the frequency increases to approach the response frequency (i.e., the inverse of the response time) of the sensor. In particular, the piezoresistive mode can no longer detect the signal once the frequency exceeds 60 Hz (Fig. S8b, Supporting Information). The response time of the piezoresistive mode is determined to be 15 ms (Fig. S9, Supporting Information), which is limited by the viscoelasticity of PDMS [44]. This limitation may be addressed by exploiting different elastomeric substrates with hierarchical structures for high-frequency applications [61]. In contrast, the piezoelectric layer presents a suitable alternative to detect dynamic high-frequency stimuli. The dynamically changing pressure reorients the aligned molecular dipoles in the piezoelectric layer to cause an internal piezoelectric potential. When externally connected, the free charge carriers could flow from the higher to the lower potential region through the metal electrodes to balance the internal piezoelectric potential, thus giving rise to an impulse signal. The impulsive voltage output from the piezoelectric layer is only present when there is a dynamically changing signal (Fig. S8d, Supporting Information). As the frequency of the pressure loading reduces to a lower value such as below 0.05 Hz, the generated instantaneous impulse becomes even smaller than the noise (Fig. S8c, Supporting Information). Nevertheless, both sensing modes exhibit a highly linear and sensitivity response in their frequency range, i.e., a sensitivity of 14.5 kPa^{-1}over the frequency range ($<$ 60 Hz) for the piezoresistive mode and a sensitivity of 1.62 V/kPa over the frequency range from 0.05 to 700 Hz for the piezoelectric mode (Fig. 3d). The highly linear and sensitive performance ($S_{\text{Piezoresistive}} =$ 14.5 kPa^{-1}, $S_{\text{Piezoelectric}} = 1.62$ V/kPa) of the dual-mode sensor over a broad pressure (0.015–9 kPa) and frequency range (0–700 Hz) compares favorably with the previous literature reports (Fig. 3e and f) [62–71]. Most of the previously reported sensors only work within a narrow frequency range [39,47,63], i.e., below 100 Hz. Although a few sensors demonstrate a relatively wide frequency range [44,45,63], their sensitivities are significantly lower than ours. Together with the excellent linearity, our dual-mode sensor exhibits unprecedented sensing capabilities.

Simultaneous measurements of the high-fidelity pressure from both the piezoelectric and piezoresistive modes further allow for the deconvolution of the complex loading processes. The simultaneous measurement setup includes a semiconductor parameter analyzer (4200-SCS, Keithley) and piezoelectric data acquisition system (KSI) (Fig. S10, Supporting Information). The challenge lies in the differentiation of the rate, direction, and magnitude of the dynamically changing stimuli in the complex loading process. The concept is first illustrated in a simple bending process. The bending strain applied on the specimen is gradually reduced from 3 % to 0 % at a step size of 1 % and an unloading rate of 2 %/s in the first bending process (Fig. S11a, Supporting Information), whereas it is reduced from 3 % to −1.5 % at a step size of 1.5 % and an unloading rate of 2 %/s in the second bending process (Fig. S11c, Supporting Information). Although the two bending processes are different in the unloading step size, the output voltage signals from piezoelectric sensors are indistinguishable due to the same unloading rate (Fig. S11bd, Supporting Information). The capability of the piezoelectric mode to detect the loading or unloading rate relies on its frequency-dependent response. Regardless of unloading or reverse of bending led the free-charge carriers to return from the negative to the positive potential across the external circuit, giving rise to a negative peak. Therefore, the piezoelectric mode cannot differentiate the unloading (1 %–0 % in the 1st process) from the reverse loading (0 % to −1.5 % in the 2nd process), failing to inform the ultimate stress or strain state of the specimen. Meanwhile, the piezoresistive mode cannot provide the information on the loading direction and rate. Therefore, the output from the piezoresistive sensor remained the same regardless the specimen is bent to the left or right at different step loading rates (Figs. S12a–c, Supporting Information). However, the synergistic effect between the piezoelectric and piezoresistive modes in the dual-mode sensor may present opportunities to deconvolute various aspects of the complex loading process, including loading rate, direction, magnitude, and duration.

As a proof-of-concept demonstration, the dual-mode sensor is used to deconvolute the various aspects (e.g., loading direction, rate, and magnitude), which is then exploited to reproduce the real-time varying pressure loading process (Fig. 4a and b). The loading direction is defined as positive (or negative) as the pressure is applied on the top (or bottom) surface of the sensor. In brief, the loading direction can be first informed by combining the sign of piezoelectric signal and changing trend of the piezoresistive signal. When the piezoresistive signal is increasing, the positive (or negative) piezoelectric signal leads to a positive (or negative) loading. When the piezoresistive signal is decreasing, the positive (or negative) piezoelectric signal leads to an unloading process from negative (or positive) loading. Next, the magnitude and duration of the pressure can be obtained from the piezoresistive signals. The loading rate can then be determined from the first peak of the piezoelectric pulse. The steps start with the recording of both the piezoelectric and piezoresistive signals from the dual-mode sensor during the pressure loading (Fig. 4a). The increase in the piezoresistive current from zero together with a positive piezoelectric pulse indicates a positive pressure loading. As the magnitude of the pressure (P) scales linearly with the normalized current change ($\Delta I/I_0$) with a slope of 14.5 kPa^{-1} according to the relationship $\Delta I/I_0 = (P\text{-}0.015) \times 14.5$, the measured $\Delta I/I_0$ of 29.6 yields a pressure of 2.06 kPa. The loading rate (r) to ramp up the pressure to 2.06 kPa can be determined from the piezoelectric signal, since it scales linearly with the first peak of the piezoelectric pulse (V_{out}). Because the calibrated slope is 0.23 V/(kPa/s) and the loading rate intercept is 0.1 kPa/s (Fig. S13, Supporting Information), the linear relationship is expressed as $V_{\text{out}} = (r\text{-}0.1) \times 0.23$. The measured V_{out} of 0.22 V then gives a loading rate of 1.05 kPa/s. The pressure is maintained at 2.06 kPa for ca. 10 s, as indicated by the piezoresistive signal. Next, the decrease in the piezoresistive current to zero together with a negative piezoelectric pulse indicates two pressure unloading steps to reduce the pressure down to 0 kPa. The increase in the piezoresistive current from zero together with a negative piezoelectric pulse then indicates two negative pressure loading steps (i.e., reverse loading steps). Following a loading rate of 2.08 kPa/s and 2.05 kPa/s, respectively, the

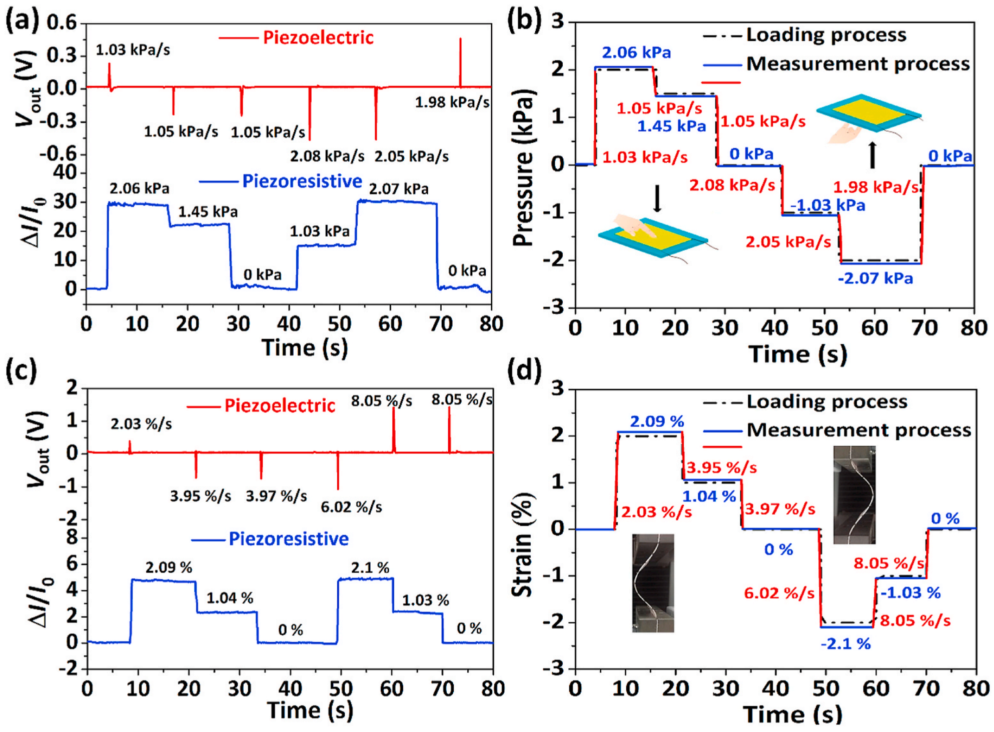

Fig. 4. Application of dual-mode sensors to deconvolute various aspects (e.g., loading direction, rate, and magnitude) of a complex pressure loading or bending process. a) Measured piezoelectric voltage and piezoresistive current as the pressure loading process varies the magnitude, rate, and direction. b) Comparison of the complex pressure loading process between the actual and measured processes. c) Measured piezoelectric voltage and piezoresistive current as the bending process varies the strain, rate, and direction. d) Comparison of the complex bending process between the actual and measured processes.

magnitude of the pressure increases to 1.03 kPa and then to 2.07 kPa during the two reverse loading steps. Finally, the decrease in the piezoresistive current to zero together with a positive piezoelectric pulse indicates a reverse unloading process to reduce the pressure down to 0 kPa. Compared to the actual pressure loading process (i.e., the black dotted line in Fig. 4b), the reproduced loading and unloading steps during the entire process measured by the dual-mode sensor only show a negligibly small error of less than 5 %.

The complex bending process can also be accurately reproduced by the dual-mode sensor with simultaneous measurements of piezoelectric and piezoresistive signals (Fig. 4c). Similar to the loading direction in the above example, the bending direction is determined first with the positive for left and negative for right. Next, the magnitude of the bending strain ϵ is calculated from the normalized relative piezoresistive current $\Delta I/I_0$, according to the linear relationship $\Delta I/I_0 = (\epsilon\text{-}0.02\%) \times 2.16$. For instance, the bending strain of 2.09 % is obtained as the normalized relative piezoresistive current $\Delta I/I_0$ is measured to be 0.45. Meanwhile, the linear dependence of the strain rate (S) on the first peak of the piezoelectric pulse V_{out} leads to a strain rate of 2.03 %/s, as V_{out} is measured to be 0.35 V according to $V_{out} = (S\text{-}0.05) \times 0.18$. Following a similar analysis, the bending strain applied to the specimen decreases to 0 % during an unloading step. After the specimen bends to the right, it is loaded reversely to a strain of 2.1 %, followed by two unloading steps back to 0 % at an unloading rate of 8.05 %/s. The reproduced bending process also accurately captures the various aspects of the actual deformation process (Fig. 4d).

Precisely capturing the real-time dynamically changing stimuli creates application opportunities for the dual-mode sensor in intelligent robots [72] and future human-machine interfaces. The dual-mode sensor is first demonstrated as a smart manipulator in intelligent factories to grab and transport delicate objects on the assembly line toward the former application (Fig. 5a). Simply attaching the dual-mode sensor on the joint of the manipulator allows it to self-monitor its operation stage (Fig. 5b). The bending direction, rate, and angle of the manipulator can be decoded from the comprehensive analysis of the measured piezoelectric and piezoresistive signals. Realizing the full potential of future human-machine interfaces also hinges on the real-time monitoring of both the speed and gesture, because the range of motion controls is significantly limited by the simple gesture/motion detection. Applying the dual-mode sensor on the human wrist easily expands the previous motion detection into various aspects of motions, including motion direction, range, and speed (Fig. 5c). Furthermore, the application of the flexible dual-mode sensor for an interactive human-machine interface demonstrates its capability to control the manipulator for specific gestures (Fig. 5c) as instructed by the human wrist in real-time (Fig. 5d). In brief, the acquired sensing signals from the wrist motions are processed by an analog-to-digital converter (ADC) after amplification and filtering. Next, the digital signals from the ADC module are further received and processed by the micro-controller, which are then sent to a workstation PC via a serial port. The classified control commands from the workstation PC are sent to the Franka Control Interface to control the Franka manipulator as instructed by the human wrist through the changes in bending direction, angle, and rate (Movie S1, Supporting Information).

Supplementary data related to this article can be found at https://doi.org/10.1016/j.nanoen.2020.105337.

3. Conclusion

In summary, we have demonstrated a highly linear and sensitive bioinspired dual-mode sensor that combines the top piezoelectric module with a bottom piezoresistive module in an interlocked manner with pyramidal microstructures. Through a comprehensive set of theoretical/numerical design tools, the optimized pyramidal microstructures are demonstrated to induce a large stress/strain variation along the thickness direction of the piezoelectric film and an increased contact area change in the interlocked piezoresistive module for enhanced sensitivity. By utilizing the synergistic effect between the piezoelectric and piezoresistive signals to static and dynamic stimuli, the flexible dual-mode sensor exhibits a highly linear and sensitivity response over a broad pressure and frequency range. Most importantly, the dual-mode sensor can deconvolute various aspects of the complex loading process (e.g., loading rate, magnitude, and direction), which is explored to accurately reproduce the complex loading process. Proof-of-concept

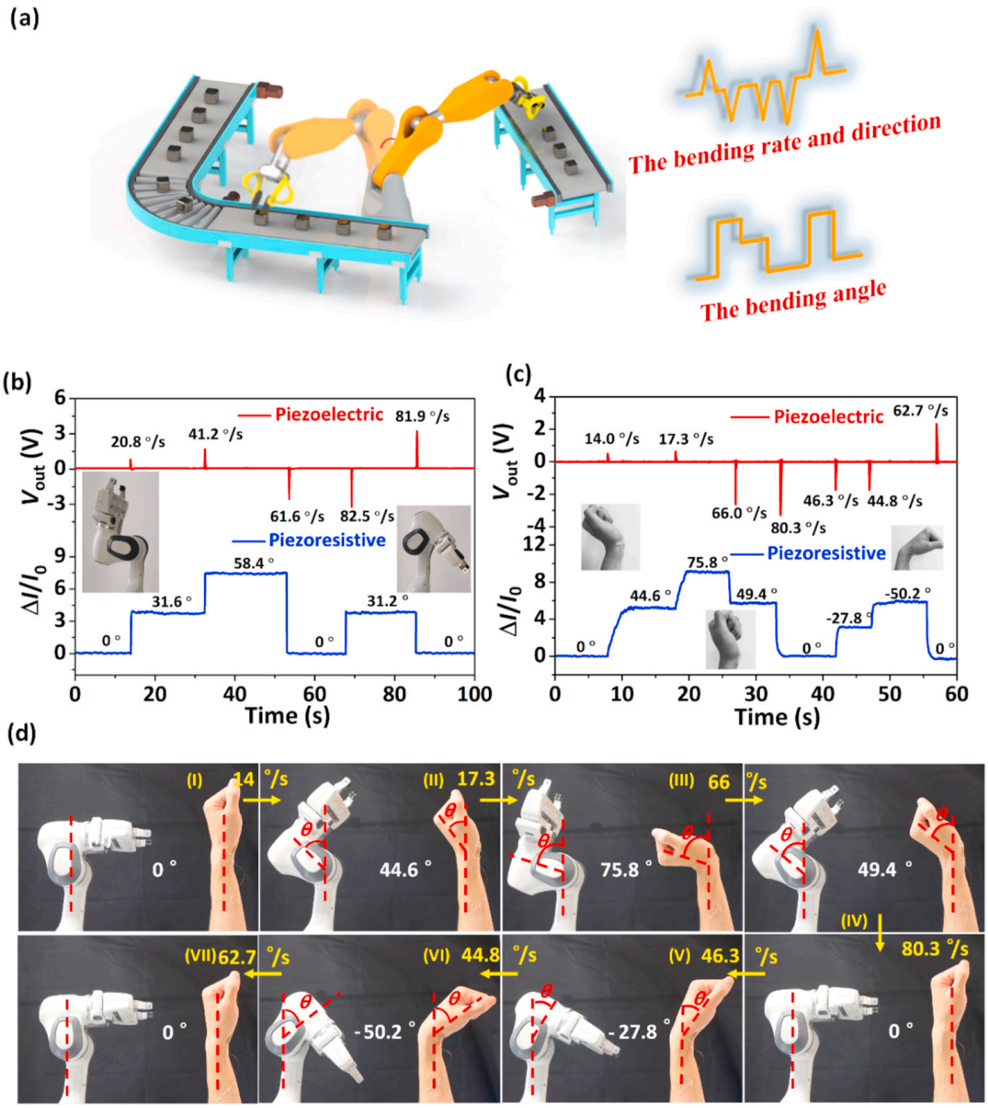

Fig. 5. Applications of the dual-mode sensors as a smart manipulator or human motion decoder for future intelligent robots and human-machine interfaces. a) Schematic diagram of the smart manipulator grabbing and transporting delicate objects on the assembly line. Measured piezoelectric voltage and piezoresistive current from the dual-mode sensor during the operation of the b) smart manipulator and c) human motion decoder.d) Demonstration of the flexible dual-mode sensor for real-time, continuous control of a manipulator via the recoded motion signals from the human wrist, corresponding to the complex loading process in c). (I) The bending angle is increased first (I) from 0° to 44.6° and then (II) from 44.6° to 75.8° at bending rates of 14 °/s and 17.3 °/s in the first and second steps, respectively. Next, the bending angle is reduced first (III) from 75.8° to 49.4° and then (IV) from 49.4° to 0° at bending rates of 66 °/s and 80.3 °/s in the first and second steps, respectively. Following the forward bending, the reverse bending angle is increased first (V) from 0° to −27.8° and then (VI) from −27.8° to −50.2° at bending rates of 46.3 °/s and 44.8 °/s in the first and second steps, respectively. (VII) Lastly, the bending angle is reduced from −50.2° to 0° at a bending rate of 62.7 °/s.

demonstrations also include smart manipulators in intelligent factories and motion decoders for exploiting various aspects of motions. Such demonstrated capabilities enable the dual-mode sensor to be integrated with various objects to create application opportunities in intelligent soft robotic systems, interactive wearable electronics, and future human-machine interfaces.

4. Experimental section

4.1. Preparation of microstructured P(VDF-TrFE) piezoelectric films

The P(VDF-TrFE) powder (Piezotech) was first mixed with N, N-Dimethylformamide (DMF) at a molar ratio of 70 to 30. Stirring the mixture at room temperature for 2 h yielded a uniform solution. Casting the uniform solution on the Si mold with pyramid microstructures, followed by annealing at 120 °C for 2 h to enhance crystallinity, prepared the P(VDF-TrFE) film. After peeling off from the Si mold, the microstructured film was then polarized by placing it in a silicone oil bath at a high electric field of 60 MV/m for half an hour. High piezoelectric properties were obtained in the resulting film (e.g., $d_{33} = 23$ pC/N^{-1}).

4.2. Synthesis of reduced graphene oxide (rGO) and GO

GO was prepared by a modified Hummers' method. In brief, after adding the graphite powder (1 g) into the solution of concentrated H_2SO_4 (25 mL) and $NaNO_3$ (0.5 g), the mixture was oxidized by $KMnO_4$ (4 g) under vigorous stirring for 30 min in an ice water bath. Next, the mixture was allowed to react for 1.5 h while keeping the temperature below 281 K. Moving the mixture into a water bath at 35–37 °C for 1.5 h obtained a brown suspension. After adding the cold distilled water of 70 mL, the mixture was heated to 90 °C for 30 min. Next, the mixture was further diluted with distilled water of 30 mL and treated with 30 % H_2O_2 of 5 mL. After the suspension turned bright yellow, the GO dispersion was centrifuged at 1000 rpm for 40 min twice to remove the unexfoliated particles and then centrifuged at 8000 rpm for 40 min twice to remove the small flake GO. Lastly, centrifuging at 10,000 rpm produced the GO dispersion.

The rGO solution was fabricated using a two-step freeze-drying and thermal annealing method. The GO powder was first prepared using a freeze-casting process. In a typical synthesis procedure, the GO dispersion was mixed with ascorbic acid at a 1:2 wt ratio. The mixture was diluted with distilled water of 40 mL and sonicated for 30 min to obtain a uniform dispersion. The obtained solution was thermally annealed at 90 °C to yield the rGO solution.

4.3. Preparation of microstructured rGO films

The patterned Si template was first cleaned with deionized water.

The hydrophobic treatment of the patterned Si template was conducted by immersing it into a solution consisting of n-heptane of 10 mL, trimethoxyoctadecylsilane of 0.2 mL, and ethyl acetate of 0.5 mL for 2 h. Next, the Si template was annealed in an oven at 100 °C for 1 h. The microstructured PDMS film was prepared by spin-coating the mixture of PDMS (Sylgard 184, Dow Corning) with the ratio of part A to part B at 10:1 on the Si template at 1000 rpm for 20 s using an EZ4 spin coater (Schwan Technology). After degassing and curing, the microstructured PDMS film was peeled off. Next, the surface of PDMS with microstructure was treated by O_2 plasma to modify its surface with hydroxyl groups and render it hydrophilic. A thin layer of rGO film was prepared on the PDMS film by spin-coating the rGO solution at 500 rpm, followed by heating at 60 °C for 30 min. Repeating the process for 10 times led to increased thickness in the rGO film.

4.4. Fabrication of the dual-mode pressure sensors

The fabrication of the piezoelectric layer started with evaporating the gold electrodes with a thickness of 150 nm on both sides of the piezoelectric film by using an electron beam evaporator (DZS-500). Attaching the copper wires to the upper and lower gold electrodes obtained the sandwich-structured piezoelectric sensors. Next, the rGO was spin-coated at 500 rpm on one side of the piezoelectric film with the pyramid microstructure. The rGO film was connected to copper wires with the silver paint (Structureprobe, Inc.). The piezoelectric layer and piezoresistive layer were then assembled layer by layer to form a dual-mode sensor with the pyramid interlocked structure. Encapsulating the entire dual-mode pressure sensor with two PDMS films on both sides completed the fabrication of the device.

4.5. Measurements of the sensing performance of the sensors

The piezoresistive and piezoelectric signals of the sensors induced by pressure were measured by using a semiconductor parameter analyzer (4200-SCS, Keithley) and piezoelectric data acquisition system (KSI), respectively (Fig. S14, Supporting Information). The low-frequency compression and bending tests were carried out using a mechanical testing system (INSTRON LEGEND2345). The high-frequency loading was applied by driving an exciter (KSI-758MS20) on the sensor that was positioned under a cylindrical probe (KSI-758STNG3.25). The excitation signal was amplified by a power amplifier (KSI-758PA100) to drive the exciter. The magnitude of the force input to the sensor was measured by a calibrated piezoelectric force transducer (KSI-208) with a sensitivity of 4 pC/N. The output from the force transducer was passed through a charge amplifier (KSI-608A100) before being recorded by a high-precision network data analyzer (KSI–8904 N).

CRediT authorship contribution statement

Ye Qiu: Writing - original draft, Data curation, Validation. **Ye Tian:** Formal analysis, Validation. **Shenshen Sun:** Investigation. **Jiahui Hu:** Validation. **Youyan Wang:** Data curation, Validation. **Zheng Zhang:** Project administration. **Aiping Liu:** Writing - review & editing. **Huanyu Cheng:** Writing - review & editing. **Weizhan Gao:** Data curation, Validation. **Wenan Zhang:** Data curation, Validation. **Hao Chai:** Project administration. **Huaping Wu:** Writing - review & editing, Project administration.

Declaration of competing interest

The authors declare that they have no known competing financial interests or personal relationships that could have appeared to influence the work reported in this paper.

Acknowledgments

This work was supported by the National Science Foundation of China (Grant no. 11672269, 11972323, 51572242 and 51675485), the Zhejiang Provincial Natural Science Foundation of China (Grant no. LR20A020002, LR19E020004, and LR18E050002), the Fundamental Research Funds for the Provincial Universities of Zhejiang (RF-B2019004), the 111 Project (no. D16004), and the Zhejiang Lab's International Talent Fund for Young Professionals.

Appendix A. Supplementary data

Supplementary data to this article can be found online at https://doi.org/10.1016/j.nanoen.2020.105337.

References

[1] J. Dargahi, S. Najarian, Human tactile perception as a standard for artificial tactile sensing - a review, Int. J. Med. Robot. Comput. Assist. Surg. 1 (2004) 23–35, https://doi.org/10.1581/mrcas.2004.010109.

[2] A. Chortos, J. Liu, Z. Bao, Pursuing prosthetic electronic skin, Nat. Mater. 15 (2016) 937–950, https://doi.org/10.1038/nmat4671.

[3] R.S. Johansson, J.R. Flanagan, Coding and use of tactile signals from the fingertips in object manipulation tasks, Nat. Rev. Neurosci. 10 (2009) 345–359, https://doi.org/10.1038/nrn2621.

[4] P. Delmas, J.Z. Hao, L. Rodat-Despoix, Molecular mechanisms of mechanotransduction in mammalian sensory neurons, Nat. Rev. Neurosci. 12 (2011) 139–153, https://doi.org/10.1038/nrn2993.

[5] C.J. Wang, K. Sim, J. Chen, H. Kim, Z.Y. Rao, Y.H. Li, W.Q. Chen, J.Z. Song, R. Verduzco, C.J. Yu, Soft ultrathin electronics innervated adaptive fully soft robots, Adv. Mater. 30 (2018) 1706695, https://doi.org/10.1002/adma.201706695.

[6] Q. Wang, S.J. Ling, X.P. Liang, H.M. Wang, H.J. Lu, Y.Y. Zhang, Self-healable multifunctional electronic tattoos based on silk and graphene, Adv. Funct. Mater. 29 (2019) 1808695, https://doi.org/10.1002/adfm.201808695.

[7] F. Hartmann, M. Drack, M. Kaltenbrunner, Meant to merge: fabrication of stretchy electronics for robotics, Sci. Robot. 3 (2018) eaat9091, https://doi.org/10.1126/scirobotics.aat9091. UNSP.

[8] X. Han, X. Chen, X. Tang, Y.-L. Chen, J.-H. Liu, Q.-D. Shen, Flexible polymer transducers for dynamic recognizing physiological signals, Adv. Funct. Mater. 26 (2016) 3640–3648, https://doi.org/10.1002/adfm.201600008.

[9] Y.H. Chen, S.Y. Lu, S.S. Zhang, Y. Li, Z. Qu, Y. Chen, B.W. Lu, X.Y. Wang, X. Feng, Skin-like biosensor system via electrochemical channels for noninvasive blood glucose monitoring, Sci. Adv. 3 (2017), e1701629, https://doi.org/10.1126/sciadv.1701629.

[10] X. Ning, X.G. Yu, H.L. Wang, R.J. Sun, R.E. Corman, H.B. Li, C.M. Lee, Y.G. Xue, A. Chempakasseril, Y. Yao, Z.Q. Zhang, H.W. Luan, Z.Z. Wang, W. Xia, X. Feng, R. H. Ewoldt, Y.G. Huang, Y.H. Zhang, J.A. Rogers, Mechanically active materials in three-dimensional mesostructures, Sci. Adv. 4 (2018) eaat8313, https://doi.org/10.1126/sciadv.aat8313.

[11] C.Y. Qu, S.Q. Wang, L. Liu, Y.Y. Bai, L.H. Li, F.Q. Sun, M.M. Hao, T. Li, Q.F. Lu, L. L. Li, S.J. Qin, T. Zhang, Bioinspired flexible volatile organic compounds sensor based on dynamic surface wrinkling with dual-signal response, Small 15 (2019) 1900216, https://doi.org/10.1002/smll.201900216.

[12] K.I. Jang, H.U. Chung, S. Xu, C.H. Lee, H.W. Luan, J. Jeong, H.Y. Cheng, G.T. Kim, S.Y. Han, J.W. Lee, J. Kim, M. Cho, F.X. Miao, Y.Y. Yang, H.N. Jung, M. Flavin, H. Liu, G.W. Kong, K.J. Yu, S.I. Rhee, J. Chung, B. Kim, J.W. Kwak, M.H. Yun, J. Y. Kim, Y.M. Song, U. Paik, Y.H. Zhang, Y. Huang, J.A. Rogers, Soft network composite materials with deterministic and bio-inspired designs, Nat. Commun. 6 (2015) 6566, https://doi.org/10.1038/ncomms7566.

[13] W. Zhai, Q.J. Xia, K.K. Zhou, X.Y. Yue, M.N. Ren, G.Q. Zheng, K. Dai, C.T. Liu, C. Y. Shen, Multifunctional flexible carbon black/polydimethylsiloxane piezoresistive sensor with ultrahigh linear range, excellent durability and oil/water separation capability, Chem. Eng. J. 372 (2019) 373–382, https://doi.org/10.1016/j.cej.2019.04.142.

[14] J.F. Gao, B. Li, X.W. Huang, L. Wang, L.W. Lin, H. Wang, H.G. Xue, Electrically conductive and fluorine free superhydrophobic strain sensors based on SiO2/graphene-decorated electrospun nanofibers for human motion monitoring, Chem. Eng. J. 373 (2019) 298–306, https://doi.org/10.1016/j.cej.2019.05.045.

[15] K. Parida, V. Bhavanasi, V. Kumar, R. Bendi, P.S. Lee, Self-powered pressure sensor for ultra-wide range pressure detection, Nano Res. 10 (2017) 3557–3570, https://doi.org/10.1007/s12274-017-1567-6.

[16] L.H. Yu, Y.Y. Yi, T. Yao, Y.Z. Song, Y.R. Chen, Q.C. Li, Z. Xia, N. Wei, Z.N. Tian, B. Q. Nie, L. Zhang, Z.F. Liu, J.Y. Sun, All VN-graphene architecture derived self-powered wearable sensors for ultrasensitive health monitoring, Nano Res. 12 (2019) 331–338, https://doi.org/10.1007/s12274-018-2219-1.

[17] B. Tian, W.J. Yao, P. Zeng, X. Li, H.J. Wang, L. Liu, Y. Feng, C.S. Luo, W. Wu, All-printed, low-cost, tunable sensing range strain sensors based on Ag nanodendrite conductive inks for wearable electronics, J. Mater. Chem. C 7 (2019) 809–818, https://doi.org/10.1039/c8tc04753g.

[18] Z. Liu, H. Li, B.J. Shi, Y.B. Fan, Z.L. Wang, Z. Li, Wearable and implantable triboelectric nanogenerators, Adv. Funct. Mater. 29 (2019) 1808820, https://doi.org/10.1002/adfm.201808820.

[19] Y.J. Hong, H. Jeong, K.W. Cho, N. Lu, D.H. Kim, Wearable and implantable devices for cardiovascular healthcare: from monitoring to therapy based on flexible and stretchable electronics, Adv. Funct. Mater. 29 (2019) 1808247, https://doi.org/10.1002/adfm.201808247.

[20] S. Seyedin, P. Zhang, M. Naebe, S. Qin, J. Chen, X.A. Wang, J.M. Razal, Textile strain sensors: a review of the fabrication technologies, performance evaluation and applications, Mater. Horizons. 6 (2019) 219–249, https://doi.org/10.1039/c8mh01062e.

[21] S.Y. Huang, Y. Liu, Y. Zhao, Z.F. Ren, C.F. Guo, Flexible electronics: stretchable electrodes and their future, Adv. Funct. Mater. 29 (2019) 1805924, https://doi.org/10.1002/adfm.201805924.

[22] J. Zhu, J.J. Fox, N. Yi, H. Cheng, Structural design for stretchable microstrip antennas, ACS Appl. Mater. Interfaces 11 (2019) 8867–8877, https://doi.org/10.1021/acsami.8b22021.

[23] T. Ha, J. Tran, S.Y. Liu, H. Jang, H. Jeong, R. Mitbander, H. Huh, Y.T. Qiu, J. Duong, R.L. Wang, P.L. Wang, A. Tandon, J. Sirohi, N.S. Lu, A chest-laminated ultrathin and stretchable e-tattoo for the measurement of electrocardiogram, seismocardiogram, and cardiac time intervals, Adv. Sci. 6 (2019) 1900290, https://doi.org/10.1002/advs.201900290.

[24] K.L. Xia, C.Y. Wang, M.Q. Jian, Q. Wang, Y.Y. Zhang, CVD growth of fingerprint-like patterned 3D graphene film for an ultrasensitive pressure sensor, Nano Res. 11 (2018) 1124–1134, https://doi.org/10.1007/s12274-017-1731-z.

[25] H.H. Singh, N. Khare, Flexible ZnO-PVDF/PTFE based piezo-tribo hybrid nanogenerator, Nano Energy 51 (2018) 216–222, https://doi.org/10.1016/j.nanoen.2018.06.055.

[26] N.R. Alluri, S. Selvarajan, A. Chandrasekhar, B. Saravanakumar, J.H. Jeong, S.-J. Kim, Piezoelectric BaTiO3/alginate spherical composite beads for energy harvesting and self-powered wearable flexion sensor, Compos. Sci. Technol. 142 (2017) 65–78, https://doi.org/10.1016/j.compscitech.2017.02.001.

[27] G. Ge, Y.C. Cai, Q.C. Dong, Y.Z. Zhang, J.J. Shao, W. Huang, X.C. Dong, A flexible pressure sensor based on rGO/polyaniline wrapped sponge with tunable sensitivity for human motion detection, Nanoscale 10 (2018) 10033–10040, https://doi.org/10.1039/c8nr02813c.

[28] C.M. Boutry, M. Negre, M. Jorda, O. Vardoulis, A. Chortos, O. Khatib, Z.N. Bao, A hierarchically patterned, bioinspired e-skin able to detect the direction of applied pressure for robotics, Sci. Robot. 3 (2018), eaau6914, https://doi.org/10.1126/scirobotics.aau6914.

[29] H.T. Chen, Z.M. Su, Y. Song, X.L. Cheng, X.X. Chen, B. Meng, Z.J. Song, D.M. Chen, H.X. Zhang, Omnidirectional bending and pressure sensor based on stretchable cnt-pu sponge, Adv. Funct. Mater. 27 (2017) 1604434, https://doi.org/10.1002/adfm.201604434.

[30] C.Y. Wang, K.L. Xia, H.M. Wang, X.P. Liang, Z. Yin, Y.Y. Zhang, Advanced carbon for flexible and wearable electronics, Adv. Mater. 31 (2019) 1801072, https://doi.org/10.1002/adma.201801072.

[31] L. Cheng, Wei Qian, L. Wei, H.J. Zhang, T.Y. Zhao, M. Li, A.P. Liu, H.P. Wu, A highly sensitive piezoresistive sensor with interlocked graphene microarrays for meticulous monitoring of human motions, J. Mater. Chem. C (2020), https://doi.org/10.1039/d0tc02539a.

[32] N. Bai, L. Wang, Q. Wang, J. Deng, Y. Wang, P. Lu, J. Huang, G. Li, Y. Zhang, J. Yang, K. Xie, X. Zhao, C.F. Guo, Graded intrafillable architecture-based iontronic pressure sensor with ultra-broad-range high sensitivity, Nat. Commun. 11 (2020) 209, https://doi.org/10.1038/s41467-019-14054-9.

[33] Y. Lee, J. Park, S. Cho, Y.E. Shin, H. Lee, J. Kim, J. Myoung, S. Cho, S. Kang, C. Baig, H. Ko, Flexible ferroelectric sensors with ultrahigh pressure sensitivity and linear response over exceptionally broad pressure range, ACS Nano 12 (2018) 4045–4054, https://doi.org/10.1021/acsnano.8b01805.same as.

[34] Q. Zhai, S. Gong, Y. Wang, Q. Lyu, Y. Liu, Y. Ling, J. Wang, G.P. Simon, W. Cheng, Enokitake mushroom-like standing gold nanowires toward wearable noninvasive bimodal glucose and strain sensing, ACS Appl. Mater. Interfaces 11 (2019) 9724–9729, https://doi.org/10.1021/acsami.8b19383.

[35] Y. Wang, S. Gong, D. Gomez, Y. Ling, L.W. Yap, G.P. Simon, W. Cheng, Unconventional janus properties of enokitake-like gold nanowire films, ACS Nano 12 (2018) 8717–8722, https://doi.org/10.1021/acsnano.8b04748.

[36] J.-H. Lee, K.Y. Lee, M.K. Gupta, T.Y. Kim, D.-Y. Lee, J. Oh, C. Ryu, W.J. Yoo, C.-Y. Kang, S.-J. Yoon, J.-B. Yoo, S.-W. Kim, Highly stretchable piezoelectric-pyroelectric hybrid nanogenerator, Adv. Mater. 26 (2014) 765–769, https://doi.org/10.1002/adma.201303570.

[37] H. Chen, Z. Su, Y. Song, X. Cheng, X. Chen, B. Meng, Z. Song, D. Chen, H. Zhang, Omnidirectional bending and pressure sensor based on stretchable CNT-PU sponge, Adv. Funct. Mater. 27 (2017) 1604434, https://doi.org/10.1002/adfm.201604434.

[38] Y.J. Hong, H. Jeong, K.W. Cho, N. Lu, D.-H. Kim, Wearable and implantable devices for cardiovascular healthcare: from monitoring to therapy based on flexible and stretchable electronics, Adv. Funct. Mater. 29 (2019) 1808247, https://doi.org/10.1002/adfm.201808247.

[39] D.I. Kim, T.Q. Trung, B.U. Hwang, J.S. Kim, S. Jeon, J. Bae, J.J. Park, N.E. Lee, A sensor array using multifunctional field-effect transistors with ultrahigh sensitivity and precision for bio-monitoring, Sci. Rep. 5 (2015) 12705, https://doi.org/10.1038/srep12705.

[40] Z.F. Chen, Z. Wang, X.M. Li, Y.X. Lin, N.Q. Luo, M.Z. Long, N. Zhao, J.B. Xu, Flexible piezoelectric-induced pressure sensors for static measurements based on nanowires/graphene heterostructures, ACS Nano 11 (2017) 4507–4513, https://doi.org/10.1021/acsnano.6b08027.

[41] S. Gao, X.Y. Wu, H.B. Ma, J. Robertson, A. Nathan, Ultrathin multifunctional graphene-pvdf layers for multidimensional touch interactivity for flexible displays, ACS Appl. Mater. Interfaces 9 (2017) 18410–18416, https://doi.org/10.1021/acsami.7b03437.

[42] S.H. Shin, D.H. Park, J.Y. Jung, M.H. Lee, J. Nah, Ferroelectric zinc oxide nanowire embedded flexible sensor for motion and temperature sensing, ACS Appl. Mater. Interfaces 9 (2017) 9233–9238, https://doi.org/10.1021/acsami.7b00380.

[43] J. Park, M. Kim, Y. Lee, H.S. Lee, H. Ko, Fingertip skin-inspired microstructured ferroelectric skins discriminate static/dynamic pressure and temperature stimuli, Sci. Adv. 1 (2015), e1500661, https://doi.org/10.1126/sciadv.1500661.

[44] M. Ha, S. Lim, J. Park, D.S. Um, Y. Lee, H. Ko, Bioinspired interlocked and hierarchical design of ZnOnanowire arrays for static and dynamic pressure-sensitive electronic skins, Adv. Funct. Mater. 25 (2015) 2841–2849, https://doi.org/10.1002/adfm.201500453.

[45] K.Y. Chun, Y.J. Son, E.S. Jeon, S. Lee, C.S. Han, A self-powered sensor mimicking slow- and fast-adapting cutaneous mechanoreceptors, Adv. Mater. 30 (2018) 1706299, https://doi.org/10.1002/adma.201706299.

[46] M. Vega-Heredia, I. Muhammad, S. Ghanta, V. Ayyalusami, S. Aisyah, M.R. Elara, Multi-Sensor orientation tracking for a facade-cleaning robot, Sensors 20 (2020) 1483, https://doi.org/10.3390/s20051483.

[47] L. Persano, C. Dagdeviren, Y. Su, Y. Zhang, S. Girardo, D. Pisignano, Y. Huang, J. A. Rogers, High performance piezoelectric devices based on aligned arrays of nanofibers of poly(vinylidenefluoride-co-trifluoroethylene), Nat. Commun. 4 (2013) 1633, https://doi.org/10.1038/ncomms2639.

[48] X. Chen, H. Tian, X. Li, J. Shao, Y. Ding, N. An, Y. Zhou, A high performance P (VDF-TrFE) nanogenerator with self-connected and vertically integrated fibers by patterned EHD pulling, Nanoscale 7 (2015) 11536–11544, https://doi.org/10.1039/c5nr01746g.

[49] J.-H. Lee, H.-J. Yoon, T.Y. Kim, M.K. Gupta, J.H. Lee, W. Seung, H. Ryu, S.-W. Kim, Micropatterned P(VDF-TrFE) film-based piezoelectric nanogenerators for highly sensitive self-powered pressure sensors, Adv. Funct. Mater. 25 (2015) 3203–3209, https://doi.org/10.1002/adfm.201500856.

[50] C.L. Choong, M.B. Shim, B.S. Lee, S. Jeon, D.S. Ko, T.H. Kang, J. Bae, S.H. Lee, K. E. Byun, J. Im, Y.J. Jeong, C.E. Park, J.J. Park, U.I. Chung, Highlystretchable resistive pressure sensors using a conductive elastomeric composite on a micropyramid array, Adv. Mater. 26 (2014) 3451–3458, https://doi.org/10.1002/adma.201305182.

[51] W. Deng, X. Huang, W. Chu, Y. Chen, L. Mao, Q. Tang, W. Yang, Microstructure-based interfacial tuning mechanism of capacitive pressure sensors for electronic skin, J. Sensor. 2016 (2016) 2428305, https://doi.org/10.1155/2016/2428305.

[52] J. Park, Y. Lee, J. Hong, M. Ha, Y.-D. Jung, H. Lim, S.Y. Kim, H. Ko, Giant tunnelingpiezoresistance of composite elastomers with interlocked microdome arrays for ultrasensitive and multimodal electronic skins, ACS Nano 8 (2014) 4689–4697, https://doi.org/10.1021/nn500441k.

[53] X.D. Wang, M.L. Que, M.X. Chen, X. Han, X.Y. Li, C.F. Pan, Z.L. Wang, Full dynamic-range pressure sensor matrix based on optical and electrical dual-mode sensing, Adv. Mater. 29 (2017) 1605817, https://doi.org/10.1002/adma.201605817.

[54] E. Roh, H.-B. Lee, D.-I. Kim, N.-E. Lee, A solution-processable, omnidirectionally stretchable, and high-pressure-sensitive piezoresistive device, Adv. Mater. 29 (2017) 1703004, https://doi.org/10.1002/adma.201703004.

[55] J. Park, S. Choi, A.H. Janardhan, S.-Y. Lee, S. Raut, J. Soares, K. Shin, S. Yang, C. Lee, K.-W. Kang, H.R. Cho, S.J. Kim, P. Seo, W. Hyun, S. Jung, H.-J. Lee, N. Lee, S.H. Choi, M. Sacks, N. Lu, M.E. Josephson, T. Hyeon, D.-H. Kim, H.J. Hwang, Electromechanical cardioplasty using a wrapped elasto-conductive epicardial mesh, Sci. Transl. Med. 8 (2016) 344ra86, https://doi.org/10.1126/scitranslmed.aad8568.

[56] J. Oh, J.C. Yang, J.-O. Kim, H. Park, S.Y. Kwon, S. Lee, J.Y. Sim, H.W. Oh, J. Kim, S. Park, Pressure insensitive strain sensor with facile solution-based process for tactile sensing applications, ACS Nano 12 (2018) 7546–7553, https://doi.org/10.1021/acsnano.8b03488.

[57] L. Yang, N. Yi, J. Zhu, Z. Cheng, X. Yin, X. Zhang, H. Zhu, H. Cheng, Novel gas sensing platform based on a stretchable laser-induced graphene pattern with self-heating capabilities, J. Mater. Chem. A 8 (2020) 6487–6500, https://doi.org/10.1039/c9ta07855j.

[58] C. Pang, G.-Y. Lee, T.-i. Kim, S.M. Kim, H.N. Kim, S.-H. Ahn, K.-Y. Suh, A flexible and highly sensitive strain-gauge sensor using reversible interlocking of nanofibres, Nat. Mater. 11 (2012) 795–801, https://doi.org/10.1038/NMAT3380.

[59] J. Park, Y. Lee, J. Hong, Y. Lee, M. Ha, Y. Jung, H. Lim, S.Y. Kim, H. Ko, Tactile-direction-sensitive and stretchable electronic skins based on human-skin-inspired interlocked microstructures, ACS Nano 8 (2014) 12020–12029, https://doi.org/10.1021/nn505953t.

[60] N.R. Alluri, B. Saravanakumar, S.-J. Kim, Flexible, hybrid piezoelectric film (BaTi$_{(1-x)}$Zr$_x$O$_3$)/PVDF nanogenerator as a self-powered fluid velocity sensor, ACS Appl. Mater. Interfaces 7 (2015) 9831–9840, https://doi.org/10.1021/acsami.5b01760.

[61] S.C.B. Mannsfeld, B.C.K. Tee, R.M. Stoltenberg, C.V.H.H. Chen, S. Barman, B.V. O. Muir, A.N. Sokolov, C. Reese, Z. Bao, Highly sensitive flexible pressure sensors with microstructured rubber dielectric layers, Nat. Mater. 9 (2010) 859–864, https://doi.org/10.1038/nmat2834.

[62] S. Garain, S. Jana, T.K. Sinha, D. Mandal, Design of in situ poled Ce^{3+}doped electrospun PVDF/Graphene composite nanofibers for fabrication of nanopressure sensor and ultrasensitive acoustic nanogenerator, ACS Appl. Mater. Interfaces 8 (2016) 4532–4540, https://doi.org/10.1021/acsami.5b11356.

[63] Y. Mao, P. Zhao, G. McConohy, H. Yang, Y. Tong, X. Wang, Sponge-like piezoelectric polymer films for scalable and integratable nanogenerators and self-

powered electronic systems, Adv. Energy Mater. 4 (2014) 1301624, https://doi.org/10.1002/aenm.201301624.

[64] W. Li, S. Zhao, N. Wu, J. Zhong, B. Wang, S. Lin, S. Chen, F. Yuan, H. Jiang, Y. Xiao, B. Hu, J. Zhou, Sensitivity-enhanced wearable active voiceprint sensor based on cellular polypropylene piezoelectret, ACS Appl. Mater. Interfaces 9 (2017) 23716–23722, https://doi.org/10.1021/acsami.7b05051.

[65] S. Khan, S. Tinku, L. Lorenzelli, R.S. Dahiya, Flexible tactile sensors using screen-printed P(VDF-TrFE) and MWCNT/PDMS composites, IEEE Sensor. J. 15 (2015) 3146–3155, https://doi.org/10.1109/JSEN.2014.2368989.

[66] J. Park, Y. Lee, S. Lim, Y. Lee, Y. Jung, H. Lim, H. Ko, Ultrasensitive piezoresistive pressure sensors based on interlocked micropillar arrays, BioNanoScience 4 (2014) 349–355, https://doi.org/10.1007/s12668-014-0151-8.

[67] C. Pang, G.Y. Lee, T.I. Kim, S.M. Kim, H.N. Kim, S.H. Ahn, K.Y. Suh, A flexible and highly sensitive strain-gauge sensor using reversible interlocking of nanofibres, Nat. Mater. 11 (2012) 795–801, https://doi.org/10.1038/NMAT3380.

[68] L. Qiu, M.B. Coskun, Y. Tang, J.Z. Liu, T. Alan, J. Ding, V.T. Truong, D. Li, Ultrafast dynamic piezoresistive response of graphene-based cellular elastomers, Adv. Mater. 28 (2016) 194, https://doi.org/10.1002/adma.201503957.

[69] J. Ge, L. Sun, F.R. Zhang, Y. Zhang, L.A. Shi, H.Y. Zhao, H.W. Zhu, H.L. Jiang, S. H. Yu, A stretchable electronic fabric artificial skin with pressure-, lateral strain-, and flexion-sensitive properties, Adv. Mater. 28 (2016) 722–728, https://doi.org/10.1002/adma.201504239.

[70] H. Park, Y.R. Jeong, J. Yun, S.Y. Hong, S. Jin, S.J. Lee, G. Zi, J.S. Ha, Stretchable array of highly sensitive pressure sensors consisting of polyaniline nanofibers and au-coated polydimethylsiloxane micropillars, ACS Nano 9 (2015) 9974–9985, https://doi.org/10.1021/acsnano.5b03510.

[71] Y.B. Wan, Z.G. Qiu, Y. Hong, Y. Wang, J.M. Zhang, Q.X. Liu, Z.G. Wu, C.F. Guo, A highly sensitive flexible capacitive tactile sensor with sparse and high-aspect-ratio microstructures, Adv. Electron. Mater. 4 (2018) 1700586, https://doi.org/10.1002/aelm.201700586.

[72] W.C. Chang, C.H. Wu, Eye-in-hand vision-based robotic bin-picking with active laser projection, Int. J. Adv. Manuf. Technol. 85 (2016) 2873–2885, https://doi.org/10.1007/s00170-015-8120-0.

Ye Qiu received her Bachelor of Taizhou University in 2015. She is currently pursuing a Ph.D. degree in the College of Mechanical Engineering at Zhejiang University of Technology. She worked as a visiting scholar in Department of Mechanical Engineering at University of Colorado Boulder from 2018 to 2019. Her research interests include flexible electronics and smart materials/structures.

Dr. Ye Tian is an Assistant Professor in the College of Mechanical Engineering at Zhejiang University of Technology, China. She received her Ph.D. in Materials Science from Harbin Institute of Technology, China, in 2015. From 2016 to 2019, she worked as a postdoctoral fellow in Polymer Science and Engineering at Zhejiang University, China. Her research focuses on smart soft materials and flexible sensors.

Shenshen Sun received the B.S. degree in College of mechanical engineering from Zhejiang University of Technology, China in 2018, and he is now an M.S. candidate at Zhejiang University of Technology. His current research interests include flexible electronics and flexible robotic hand.

Jiahui Hu received his B.S. degree in Zhejiang Sci-Tech University in 2018. He is now studying for M.S. in Zhejiang University of Technology. His research interests involve flexible tactile sensor and its applications in human-machine collaboration.

Youyan Wang obtained the master degree from Zhejiang University of Technology in 2019. His research work is focused on piezoelectric materials, flexible electronics and pressure sensing.

Prof. Zheng Zhang is a full professor at Zhejiang University of Technology. He received his Ph.D. degree from Northwestern Polytechnical University in 2008. He preformed research fellow at the City University of Hong Kong from 2008 to 2009. He became a lecturer at Zhejiang University of Technology in 2009 and an associate professor at Zhejiang University of Technology in 2013. His research interests focus on smart morphing structures, composite mechanics and numerical methods such as finite element method.

Prof. Aiping Liu received her Ph.D degree in Material Science from the Harbin Institute of Technology in 2008. She worked as a postdoctoral research fellow at the Nanyang Technological University from 2009 to 2011 and a visiting scholar at the University of Texas at Austin from 2019 to 2020. She is currently a Professor in the Department of Physics at Zhejiang Sci-Tech University. Her research mainly focuses on the functional inorganic/organic material, with special emphasis on developing novel materials including graphene with sensing and actuation characteristic for wearable physical/chemical sensors and intelligent actuators.

Prof. Huanyu Cheng earned a Ph.D. degree from Northwestern University in 2015 and a Bachelor's degree from Tsinghua University in 2010. After his doctoral study, he was appointed as the Dorothy Quiggle Assistant Professor of Engineering Science and Mechanics at The Pennsylvania State University. Dr. Cheng has worked on mechanics design and advanced manufacturing of biologically inspired electronics for biomedicine. Dr. Cheng has co-authored over 80 peer-reviewed publications, and his work has been recognized through the reception of numerous awards. He also serves as an associate editor for *Computers in Biology and Medicine* and reviewer for over 120 international journals.

Weizhan Gao received his bachelor's degree in Measurement and Control Technology and Instrumentation from Qingdao University of Science and Technology, in 2019. He is currently working toward the M.S. degree in control science and engineering with Zhejiang University of Technology, China. His current research interests include human–robot interaction, machine learning, and robotics.

Prof. Wen-An Zhang received the Ph.D. degree in Control Theory and Control Engineering from Zhejiang University of Technology, China, in 2010. He has been with Zhejiang University of Technology since 2010 where he is now a professor at Department of Automation. He was a senior research associate at Department of Manufacturing Engineering and Engineering Management, City University of Hong Kong, 2010–2011. He was awarded an Alexander von Humboldt Fellowship in 2011–2012. His current research interest is multi-sensor information fusion and its applications to human-robot collaboration. He has been serving as a subject editor for Optimal Control Applications and Methods from 2016.

Dr. Hao Chai earned a Ph.D. degree from Zhejiang University of Technology in 2019 and a Bachelor's degree from Zhejiang University in 2008. After his doctoral study, he was appointed as the lecturer of Zhijiang College at Zhejiang University of Technology, Dr. Chai has worked on compound material and fracture mechanics. Dr. Chai has co-authored over 20 peer-reviewed publications, and participated in several national or provincial research projects.

Prof. Huaping Wu received his Ph. D degree in Engineering Mechanics from the Harbin Institute of Technology in 2009 and a Bachelor's degree from the Harbin Institute of Technology in 2002. He worked as a visiting scholar at the Kyoto University in 2014 and a postdoctoral research fellow at the City University of Hong Kong in 2012. He is currently a Professor in the School of Mechanical Engineering at Zhejiang University of Technology. His research mainly focuses on the mechanics of smart materials/structures, bionic machinery and bionic manufacturing, and flexible electronics devices.